

# Reaction Pathways of Water Dimer Following Single Ionization

Ivo S. Vinklárček,<sup>1</sup> Hubertus Bromberger,<sup>1</sup> Nidin Vadassery,<sup>1</sup>  
Wuwei Jin,<sup>1</sup> Jochen Küpper,<sup>1,2,3,\*</sup> and Sebastian Trippel<sup>1,2,†</sup>

<sup>1</sup>Center for Free-Electron Laser Science CFEL, Deutsches  
Elektronen-Synchrotron DESY, Notkestraße 85, 22607 Hamburg, Germany

<sup>2</sup>Center for Ultrafast Imaging, Universität Hamburg, Luruper Chaussee 149, 22761 Hamburg, Germany

<sup>3</sup>Department of Physics, Universität Hamburg, Luruper Chaussee 149, 22761 Hamburg, Germany

Water dimer (H<sub>2</sub>O)<sub>2</sub>— a vital component of the earth’s atmosphere — is an important prototypical hydrogen-bonded system. It provides direct insight into fundamental chemical and biochemical processes, e. g., proton transfer and ionic supramolecular dynamics occurring in astro- and atmospheric chemistry. Exploiting a purified molecular beam of water dimer and multi-mass ion imaging, we report the simultaneous detection of all generated ion products of (H<sub>2</sub>O)<sub>2</sub><sup>+</sup>-fragmentation following single ionization. Detailed information about ion yields and reaction energetics of 13 ion-radical pathways, 6 of which are new, of (H<sub>2</sub>O)<sub>2</sub><sup>+</sup> are presented, including strong <sup>18</sup>O-isotope effects.

## INTRODUCTION

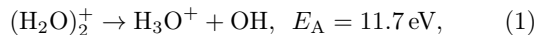
Water dimer (H<sub>2</sub>O)<sub>2</sub> is assumed to be a vivid contributor to the radiation budget [1, 2], the homogeneous condensation [3], and chemical reactions including degradation of Criegee intermediates [4] at low altitudes of the earth’s atmosphere [5–7]. Moreover, the decay of the ionic states of water clusters induced by cosmic radiation is considered essential for astrochemistry occurring on ice mantles [8–10] and plays a key role as a trigger of chemical evolution in interstellar space [11]. Therefore, as (H<sub>2</sub>O)<sub>2</sub> is the smallest water cluster, it is a favorable model system to develop a more thorough understanding of the environmental effect, i. e., hydrogen bonding’s role, in energy, charge, and mass transfer occurring in ion-radical chemistry [12–19].

Hydrogen bonding is of major importance for the vast majority of biochemical processes and chemical reactions such as proton transfer in redox reactions of light-harvesting complexes [20], or structure and topological stability of biomolecules like the double-helix structure of DNA [21, 22]. Specifically, understanding how absorbed energy dissipates and charge is re-distributed within an ionized aqueous environment is crucial in a biological context, where the interaction of biomolecules with generated low-energy electrons and ion-radicals can result in their degradation.

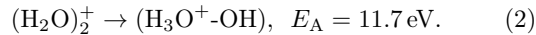
The interest in ionic supramolecular dynamics of the (H<sub>2</sub>O)<sub>2</sub> system led to several theoretical predictions [15, 16, 18, 23] of fragmentation pathways of singly and doubly charged water dimer and fragmentation energetics. These were only partly supported by the experimental results of electron-impact ionisation [24] and of Coulomb explosion [12, 14, 19, 25, 26] induced by core and valence ionization. This is not surprising, considering the experimental challenge, e. g., the interference of the products of (H<sub>2</sub>O)<sub>2</sub><sup>+</sup> fragmentation with those resulting from the fragmentation of higher clusters and isolated H<sub>2</sub>O molecules. Our experimental approach circumvents

these issues by using the electrostatic deflector [27] for the purification of (H<sub>2</sub>O)<sub>2</sub> samples and multi-mass ion imaging [28–30] to monitor all the ion-radical channels induced by strong-field ionization at once. The photoionization was set to be predominantly in the multiphoton regime to populate similar states of the (H<sub>2</sub>O)<sub>2</sub><sup>+</sup> ion as those populated from VUV/UV- or electron impact ionization.

*Ab initio* simulations revealed that the photoionization of (H<sub>2</sub>O)<sub>2</sub> through electron ejection from the four highest occupied molecular orbitals (HOMO to HOMO–3) preferably leads to proton transfer [15]. The first two ionic states of (H<sub>2</sub>O)<sub>2</sub><sup>+</sup>, i. e., the ground <sup>2</sup>A'' and the first excited <sup>2</sup>A' states, are populated by electron ejection from the two non-bonding 1b<sub>1</sub> orbitals of oxygen in the proton donor (HOMO) and the proton acceptor (HOMO–1), respectively [15, 18]. Both of these states are highly reactive, which is underlined by the estimated timescale for proton migration of less than 100 fs and 300 fs for (H<sub>2</sub>O)<sub>2</sub><sup>+</sup> in its <sup>2</sup>A'' and <sup>2</sup>A' states, respectively [15]. Recently, the timescale for the proton migration was measured as 55(20) fs in XUV-pump-XUV-probe experiments [26]. Subsequently, (H<sub>2</sub>O)<sub>2</sub><sup>+</sup> either dissociates into

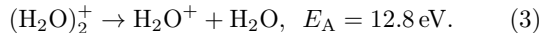


or survives as an ion-radical pair (< 40 %) [15, 16]

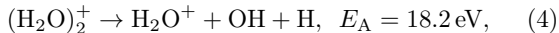


$E_A$  denotes the specific appearance energy, i. e., the minimum energy required to induce the reaction pathway.

The next two excited states of (H<sub>2</sub>O)<sub>2</sub><sup>+</sup> are populated through electron ejection from the 3a<sub>1</sub> orbital of donor (HOMO–2) and acceptor (HOMO–3) H<sub>2</sub>O followed by the prompt decay [15] into the <sup>2</sup>A'' and <sup>2</sup>A' states with subsequent dissociation *via* the channel in (1). Additional minor channels (< 20 %) either lead to an ion radical pair (H<sub>2</sub>O)<sub>2</sub><sup>+</sup> through the channel in (2) or fragmentation without proton transfer as

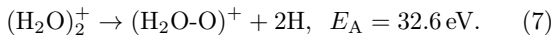
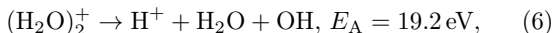
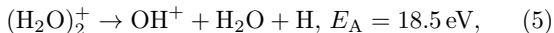


Furthermore, the electron ejection from the  $1b_2$  orbital of the donor (HOMO-4) and acceptor (HOMO-5) predominantly leads to the three-body fragmentation as



generating four species: three radical fragments and an electron. Those species should eminently increase the possibility of radiation damage in an aqueous environment [15]. The two-body fragmentation channels producing  $\text{H}_3\text{O}^+$  and  $\text{H}_2\text{O}^+$  ions participate only with a minor contribution ( $< 20\%$ ) after HOMO-4 and HOMO-5 ionization [15].

Additional channels of  $(\text{H}_2\text{O})_2^+$  fragmentation appearing at higher ionization energies were described [15, 16], i. e.,



Contrary to valence ionization, stripping of a core electron from the  $2a^1$  or  $1a^1$  orbitals, e. g., by x-ray ionization, induces direct or proton-transfer-mediated [13, 17] relaxation through local or intermolecular Auger decay [12-14, 17] and subsequent ejection of a valence electron.

Here, we exploited the combination of electrostatic deflection [31] and multi-mass imaging with a Timepix3 camera [28, 29] to yield unprecedented details into the ionic reaction pathways of the prototypical ionized  $(\text{H}_2\text{O})_2$  system. We produced a rotationally cold molecular beam of  $(\text{H}_2\text{O})_2$  with  $\sim 92\%$  purity [27] and recorded all ionic reaction products, see Methods and the supporting information (SI) for details. We directly observed all theoretically predicted fragmentation channels of  $(\text{H}_2\text{O})_2^+$  [15, 16]. Moreover, we observed multiple new fragmentation channels. The velocity-map-imaging (VMI) detection inherently provided information about the released translational energy and the rovibronic excitation of the products, which could affect subsequent reactions.

## METHODS

All experiments were performed in our recently commissioned transportable endstation for controlled-molecule experiments (eCOMO), which will be described in more detail elsewhere [32]. Fig. 1 provides a sketch of the experimental setup [32, 33]. A sample of distilled water (0.5  $\mu\text{l}$ , room temperature) was dropped on a glass-filter paper and installed in a sample holder behind the pulsed valve (Amsterdam Piezvalve) [34]. The water vapor was mixed with helium buffer gas using a stagnation pressure of 4 bar and the mixture coexpanded into vacuum in 50  $\mu\text{s}$  pulses into the source chamber; pressures with the valve on/off were  $2 \times 10^{-6}$  mbar/ $2 \times 10^{-8}$  mbar. The molecular

beam of water clusters was extracted by a first skimmer (diameter 3 mm) from the supersonic jet and further collimated by a second skimmer (diameter 1.5 mm) before entering the electrostatic deflector.

To spatially separate the water dimer clusters from the carrier helium gas as well as from isolated water molecules and larger water clusters, we used a  $b$ -type deflector [31, 35], applying a voltage of 13 kV. The dipole moments of water monomer and dimer are 1.86 D and 2.63 D, respectively [27, 36, 37]. Subsequently, the molecular beam was cut in half by a knife edge to increase both, the effective separation of water-dimer from the rest of the molecular beam and the column density [33]. The source, deflector, knife edge, and skimmers are all movable, which enabled us to optimize their positions for the separation and purification of the water-dimer clusters. The deflected molecules were intersected with short laser pulses in the interaction region of a double-sided velocity-map-imaging (VMI) spectrometer. The purity of the water-dimer beam was estimated to be 92 % by comparing the signals from known fragmentation channels compared to the background signal, i. e., water monomer, nitrogen, and oxygen, at the deflected-beam position of 2 mm.

To photoionize the molecules, we used a 800 nm Ti:Sapphire chirped-pulse-amplifier system (Coherent Astrella) operated at 1 kHz. The pulse duration is estimated to 40 fs and the pulse energies of 170  $\mu\text{J}$ . Focusing the laser beam to 53  $\mu\text{m}$  full width at half maximum (FWHM) intensity yielded a peak intensity up to  $\sim 2 \times 10^{14}$  W/cm<sup>2</sup>, corresponding to a Keldysh parameter of  $\sim 0.7$  for photoionization of  $(\text{H}_2\text{O})_2$  at  $E_i = 11.7$  eV [38].

The generated ions were then accelerated toward the detector in a perpendicular-geometry of the double-sided spectrometer [39] and projected under VMI conditions. At the end of the spectrometer, a micro-channel-plate phosphor-screen combination (MCP: Photonics, APD 3

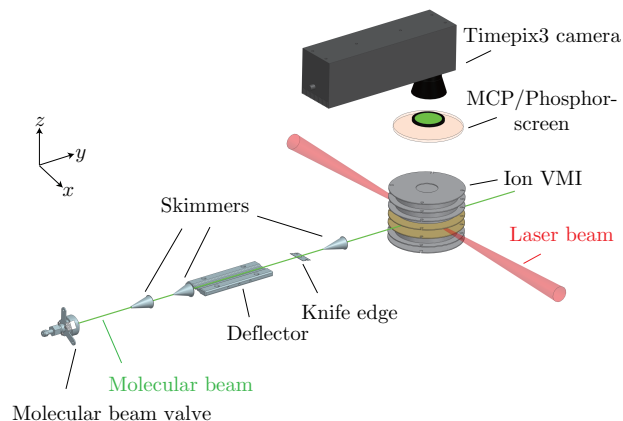


FIG. 1. Schematic picture of the endstation for controlled-molecule experiments (eCOMO) [32, 33].

PS 75/32/25/8 I 60:1 NR MGO 8"FM; PS: P47) was mounted to produce light flashes for individual ions. The flashes were detected with a Timepix3 camera [28, 40] (Amsterdam Scientific Instruments) operated and controlled by our open-source-library Pymepix [41, 42], which was also used to extract the raw physics events from the Timepix3 data stream. The detectors temporal resolution of  $\sim 1.6$  ns [28] enabled us to work in multi-mass-detection mode and to obtain the VMI images of all fragments directly by slicing, i. e., computational event selection, in the time-of-flight coordinate. The synchronization of the whole experiment is provided by a Stanford DG645 delay generator.

The plotted VMI images and beam-plot figures were background subtracted and also stripped off the contribution from the scattered/non-deflected beam by subtraction of the measured background-subtracted signal with the deflector off. The valve was operated at 200 Hz resulting in 4 successive background measurements due to the 5 times higher repetition rate of the laser with respect to the molecular-beam valve. The data were centroided by calculating the center-of-mass for each detected ion [28]. The 3D velocity (radial) and angular distributions were obtained by standard integration methods for VMI images [43]. For momentum calibration [28], we fitted the dependence of the center positions of the VMI images on the time-of-arrival and converted it to momenta applying the physical size of the ion detector and the magnification factor ( $M = v_i/v_{mb} = 0.843$ ) of the spectrometer estimated by SIMION [44]. The resulting velocity of the molecular beam is 2 km/s.

## RESULTS AND DISCUSSION

Fig. 2 depicts an overview of all acquired ions and their fragmentation channels resulting from singly and multiple-charged water dimer after strong-field ionization at 800 nm. The image shows the background subtracted ion signal for the mass-over-charge ratio and the position of arrival at the detector, see SI for details. The mass-over-charge ratio  $m/q$  is obtained by a direct transformation from the ion time of flight by  $m/q \propto t^2$ . Due to the molecular beam velocity, in this two-dimensional (2D) spectrum, all signals from species originating from the molecular-beam are shifted upward in the figure with increasing mass-over-charge ratio. Ions with zero velocity in the co-moving frame of the molecular beam appear on the dashed line. Ions in the surrounding structures centered at the dashed line are due to fragmentation of the cluster after ionization. Remaining signals are due to the ionization of the diffuse rest gas in the chamber.

For a direct comparison between the various fragments in terms of signal strength, the inset in the top graph of Fig. 2 depicts the mass spectrum obtained by summation of the signal in the lower figure along the vertical axis.

The top figure itself is a zoom into the inset to highlight weak channels.

The most prominent features in Fig. 2 are observed in the region between  $m/q = 16$  to 19 u/e, corresponding to the  $O^+$ ,  $OH^+$ ,  $H_2O^+$  and  $H_3O^+$  fragments. These fragments originated from the  $(H_2O)_2^+$  fragmentation and Coulomb-explosion channels of  $(H_2O)_2^{2+}$ . We were able to distinguish between these two sources of the signal using the 3D ion velocity detection with the Timepix3 camera [28]. Whereas  $(H_2O)_2^+$  fragmentation is represented by the central broad features around the dashed line, e. g., confined by an inner dotted ellipse at  $m/q = 17$ , the Coulomb explosion channels from  $(H_2O)_2^{2+}$  exhibit sharp ring-like – graphically-projected oval – structures assigned to “fast” ions, e. g., the area between the two dotted ellipses around  $m/q = 17$ , which will be discussed in a future publication. The strong peaks at  $m/q = 16$  to 19 u/e are also accompanied by weak signals at  $m/q = 20$  and 21 u/e assigned to the isotopologues  $H_2^{18}O^+$  and  $H_3^{18}O^+$ , respectively. The signals corresponding to the expected peak heights for isotopes in natural abundance, i. e., 0.2 % of the  $^{16}O$ -isotopologue signal, are indicated by the red horizontal lines in the mass spectrum of Fig. 2. The red bar assigned to  $H_2^{18}O^+$  was corrected upward to compensate for the contribution from the neighboring  $H_3O^+$  signal.

The second region with a strong signal, at  $m/q = 36$  u/e, corresponds to the parent ion  $(H_2O)_2^+$ . Moreover, it is accompanied by a weak peak of its isotopologue  $(H_2O-H_2^{18}O)^+$  at  $m/q = 38$  u/e, again with its expected natural-abundance signal contribution indicated by a red line in the mass spectrum. The signal strength is in very good agreement with the expected abundance. The well-resolved and clear observation of these isotopologue demonstrates the high sensitivity of our experiment. In between the two peaks there is another structure at  $m/q = 37$  u/e, which we assign to protonated water dimer  $(H_2O)_2H^+$  originating from the fragmentation of larger clusters  $(H_2O)_n^+$ ,  $n > 2$ , i. e., a remaining impurity in the experiment.

For  $m/q$  ratios of 32, 33, and 34 u/e we also observed weak but distinct signals originating in the molecular beam. These signals were assigned to  $O_2^+$ ,  $HO_2^+$  and  $(H_2O-O)^+$  ions [16], respectively. The origin of these fragments is not straightforwardly linked to any specific ion precursor. Nevertheless, measurements without purification of the reactant by deflection do not exhibit any significantly intense signals between  $m/q = 32$  and 34 u/e, see ?? in SI, which excludes their origin from larger water clusters  $(H_2O)_n$  or mixed  $(H_2O)_m(O_2)_n$  clusters. Furthermore, there are no coincidences of the  $O_2^+$ ,  $HO_2^+$ , and  $(H_2O-O)^+$  ions with  $H^+$  and  $H_2^+$  ions, see ?? in SI. Therefore, we assign the signal at 32, 33, and 34 u/e to fragmentation products of  $(H_2O)_2^+$ .

The last region with a distinguishable signal is located at  $m/q = 1-3$  u/e. We assign the signal to the hydrogen

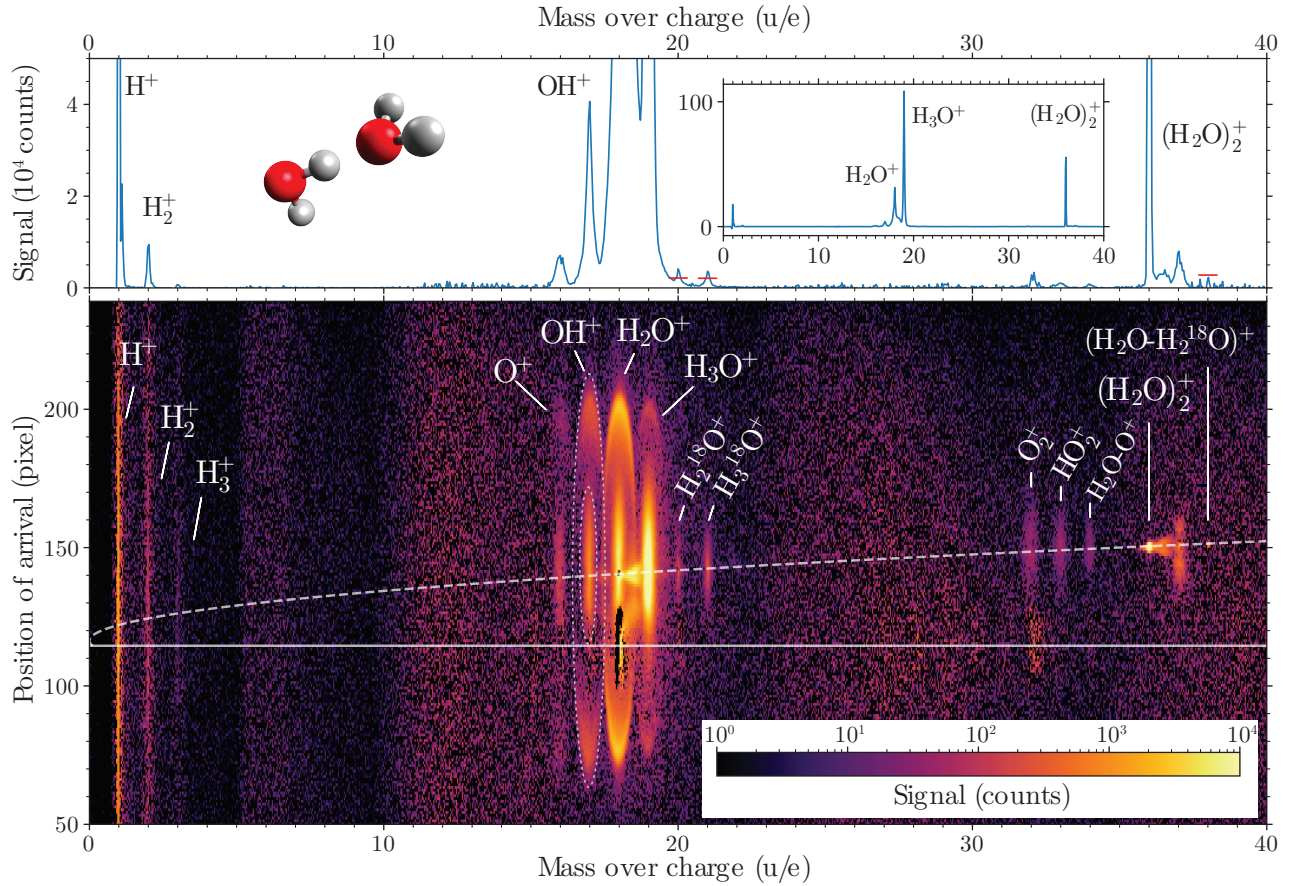


FIG. 2. Image mapping the ion signal according to the mass-over-charge ratio and the position of arrival on the detector (lower panel). The upper panel outlines the zoomed-in mass spectrum, with an inset showing the whole vertical range for reference. The observed fragments of  $(\text{H}_2\text{O})_2^+$  are  $\text{H}^+$ ,  $\text{H}_2^+$ ,  $\text{H}_3^+$ ,  $\text{O}^+$ ,  $\text{OH}^+$ ,  $\text{H}_2\text{O}^+$ ,  $\text{H}_3\text{O}^+$ ,  $\text{O}_2^+$ ,  $\text{HO}_2^+$  and  $(\text{H}_2\text{O}-\text{O})^+$ . The observed fragments of  $(\text{H}_2\text{O}-\text{H}_2^{18}\text{O})^+$  are  $\text{H}_2^{18}\text{O}^+$  and  $\text{H}_3^{18}\text{O}^+$ . The expected isotopologue-peak heights of  $\text{H}_2^{18}\text{O}^+$ ,  $\text{H}_3^{18}\text{O}^+$ , and  $(\text{H}_2\text{O}-\text{H}_2^{18}\text{O})^+$  ions are indicated by the red horizontal bars. Dotted ellipses at  $m/q = 17$  u/e are drawn to mark product regions of  $(\text{H}_2\text{O})_2^+$  fragmentation and Coulomb explosion as an example. See text for details.

ions  $\text{H}^+$ ,  $\text{H}_2^+$  and  $\text{H}_3^+$  as the isotopic natural-abundance contribution of deuterium D is below 0.02 %.

Besides the mass spectrometric information about the created ions and their signal, in VMI we also obtain insight into the energy redistribution for the specific fragmentation channels through the distributions of kinetic energy releases, which are displayed for some selected ions in Fig. 3; for comparison, see also the released-total-momentum distributions in ?? of the SI. The kinetic-energy-release spectra were obtained from the measured 3D single ion momenta assuming two-body fragmentation of the parent ion.

This is a valid assumption for the  $\text{H}_3\text{O}^+$  ions and the larger part of the  $\text{H}_2\text{O}^+$  signal according to channels (1) and (3), respectively, with the calculated kinetic-energy release equal to the total kinetic energy  $E_{\text{tr}}$ . However, the  $\text{OH}^+$  ions were produced from three-body fragmentation according to channel (5). Here, the most probable

scenario is a sequential fragmentation into  $\text{OH}^+$  with an intermediate  $\text{H}_3\text{O}$ , which further dissociates into  $\text{H}_2\text{O}$  and H. Thus, the plotted curve of the kinetic energy release in the  $\text{OH}^+$  reaction channel illustrates the kinetic energy released in the first step in the three-body fragmentation.

The low-energy peaks up to 2 eV in the  $E_{\text{tr}}$  spectra are attributed to the decay of various rovibrational states of  $(\text{H}_2\text{O})_2^+$ . The individual curve shape then results from the convolution of initial rovibronic excitation of  $(\text{H}_2\text{O})_2^+$  and subsequent statistical fragmentation. From these distributions, rovibronic excitation energies  $E_{\text{rv}}$  can be obtained assuming the conservation of energy given by  $E_{\text{total}} = E_{\text{tr}} + E_{\text{rv}}$ . In a state-selective experimental approach, such a constraint would allow for the calculation of the exact rovibronic excitation of the generated fragments. However, limitations arise in the ultrashort-pulse-ionization regime due to the spectral bandwidth of the ionizing laser,  $\sim 30$  nm in our case. Assuming that the

TABLE I. Summary of all the observed ions from  $(\text{H}_2\text{O})_2^+$  dissociation together with their relative ion yields. Our estimated appearance energies  $E_A$  are shown in the fourth column in bold, alongside the previously reported appearance energies [15, 16]. The last column shows previously reported and suggested fragmentation pathways producing the observed ions.

Fragment	Signal (counts)	Relative ion yield	$E_A$ (eV)	Reaction channel $(\text{H}_2\text{O})_2^+ \rightarrow$
$\text{H}_3\text{O}^+$	1933751	0.541(42)	11.7 [15]	$\text{H}_3\text{O}^+ + \text{OH}$ [15, 16, 19]
$\text{H}_2\text{O}^+$	630492	0.176(11)	12.8 [15] 18.2 [15]	$\text{H}_2\text{O}^+ + \text{H}_2\text{O}$ [15, 16, 19] $\text{H}_2\text{O}^+ + \text{OH} + \text{H}$ [15]
$(\text{H}_2\text{O})_2^+$	613728	0.172(8)	11.7 [15]	$\text{H}_3\text{O}^+ \cdots \text{OH}$ [15, 16, 19]
$\text{H}^+$	<sup>[a]</sup> 213905	0.06(4)	19.2 [15]	$\text{H}^+ + \text{H}_2\text{O} + \text{OH}$ [15]
$\text{OH}^+$	114390	0.032(8)	18.5 [15]	$\text{OH}^+ + \text{H}_2\text{O} + \text{H}$ [15]
$\text{O}^+$	24235	0.0068(20)	<b>21.7</b>	$\text{O}^+ + \text{H}_2\text{O} + 2\text{H}$
$\text{H}_2^+$	13947	0.0068(14)	<b>21.7</b>	$\text{H}_2^+ + \text{H}_2\text{O} + \text{O}$
$\text{H}_2^{18}\text{O}^+$	10225	0.0029(1)	-	-
$\text{H}_3^{18}\text{O}^+$	9268	0.0026(3)	-	-
$\text{O}_2^+$	6052	0.0017(3)	<b>27.6</b>	$\text{O}_2^+ + 4\text{H}$
$\text{HO}_2^+$	4206	0.0012(2)	<b>29.2</b>	$\text{HO}_2^+ + 3\text{H}$
$(\text{H}_2\text{O}-\text{O})^+$	1792	0.0005(1)	32.6 [16]/ <b>33.0</b>	$(\text{H}_2\text{O}-\text{O})^+ + 2\text{H}$ [16]
$\text{H}_3^+$	796	0.0002(3)	<b>36.5</b>	$\text{H}_3^+ + \text{HO}_2$

[a] Signal contributions by fast non-detected  $\text{H}^+$  ions are expected to be below 5 % of the integrated  $\text{H}^+$  signal.

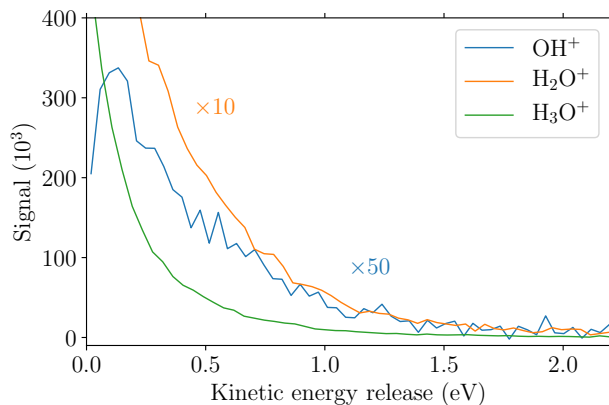


FIG. 3. Kinetic energy release of the reaction channels yielding the specified ions, assuming two-body fragmentation.

deposited energy during the  $(\text{H}_2\text{O})_2$  ionization is given by the lowest number of photons necessary to overcome the energy threshold, i. e., the appearance energy  $E_A$ , of the selected fragmentation-reaction channel and considering the effective spectral narrowing due to the multiphoton ionization, one could extract low-resolution ( $>0.04$  eV) rovibrational spectra using the dissociation threshold for each detected fragment.

Table I provides a summary of previously reported- and our new findings: A list of all detected ions from decay of  $(\text{H}_2\text{O})_2^+$  is shown in the first column. Seven of the observed ions can be linked to the already reported pathways from simulations [15, 16]. The additionally detected ions are created through previously not reported

fragmentation channels. The fragmentation pathways leading to the ejection of the newly discovered ions and those discussed in the introduction are shown in the last column. These suggested pathways are based solely on energetic arguments and thus should be further investigated, e. g., by computations or through radical detection. From our data, we cannot directly link the detected ions to the exact initial state of the ion. Nevertheless, we can count the number of detected ions and determine their relative ion yields, which are listed in the second and third columns, respectively.

Inspecting the ion yields, an intriguing observation is that whereas the signal intensity of  $\text{H}_3\text{O}^+$  is roughly three times larger than the signal of  $\text{H}_2\text{O}^+$ , the situation is changed for their isotopologues  $\text{H}_3^{18}\text{O}^+$  and  $\text{H}_2^{18}\text{O}^+$ , which exhibit comparable signal intensities, see Fig. 4. With the natural abundance of  $^{17}\text{O}$  and the sensitivity of our experiment, one would also expect to observe  $\text{H}_3^{17}\text{O}^+$  and  $\text{H}_2^{17}\text{O}^+$ . Unfortunately, these signals are hidden under the stronger signals of  $\text{H}_2^{18}\text{O}^+$  and  $\text{H}_3^{18}\text{O}^+$ , respectively. For the  $\text{H}_3\text{O}^+$  signal, a background contribution from  $\text{H}_3^{17}\text{O}^+$  is below 0.04 % and thus negligible. For the  $\text{H}_2^{18}\text{O}^+$  peak at  $m/q = 20$  u/e, a contribution by  $\text{H}_3^{17}\text{O}^+$  could be as large as 20 %. In any case, the difference of the ratios for the  $\text{H}_{2,3}^{16}\text{O}$  and  $\text{H}_{2,3}^{18}\text{O}$  signals is a surprisingly strong illustration of isotopic substitution modifying chemical-reaction pathways. This could be due to a preferred stereometric position of  $\text{H}_2^{18}\text{O}$  as a proton donor in  $(\text{H}_2\text{O})_2$ , or it could be due to a reduced proton tunneling and transfer probability between the two water moieties in the  $^{18}\text{O}$  isotopologue, which could both be a consequence of small reduced-mass changes resulting in



zero-point-energy and anharmonic-coupling effects.

On top of the qualitative analysis, the obtained relative ion yields were also utilized to estimate the appearance energies  $E_A$  of the newly detected ions and assigned channels. Within our model, the relative ion yields can be expressed as

$$P(I^+) = N \cdot \sum_k y_k^S(I^+) \cdot D(F, E_i(S)) \quad (8)$$

$N$  is a normalization factor and  $y_k^S$  is the branching ratio of the channel  $k$  producing ion  $I^+$  after ionization into an initial ionic state  $S$ . The probability to ionize into such a state  $S$  is described by the distribution  $D$  as a function of the ionization energy  $E_i$  of the state  $S$  and a parameter  $F$  corresponding to the strength of the applied external electric field [45]. The  $D$  was chosen to have an exponential character based on the strong-field ionization approximation [45]. The unknown parameters of our model, i. e.,  $F$  and the branching ratios of  $H^+$  and  $OH^+$  ions, were calibrated using the theoretical branching ratios and  $E_A$  of each channel given by Svoboda et al. [15]. We then calculated the so far unknown  $E_A$  of the less abundant ions from (8), see the SI for further details. These estimated  $E_A$  are shown in Table I including the reported ones [15, 16]. This includes the  $E_A = 33.0$  eV of  $(H_2O-O)^+$  known from [16] to be 32.6 eV. The surprisingly good agreement should be taken with caution and not as an illustration of the high precision of the presented *ad hoc* model. The calculated and reported appearance energies  $E_A$  assigned to the observed ions directly reflect the broad range of the initial energies deposited by the strong-field photoionization triggering the  $(H_2O)_2^+$ -fragmentation reactions.

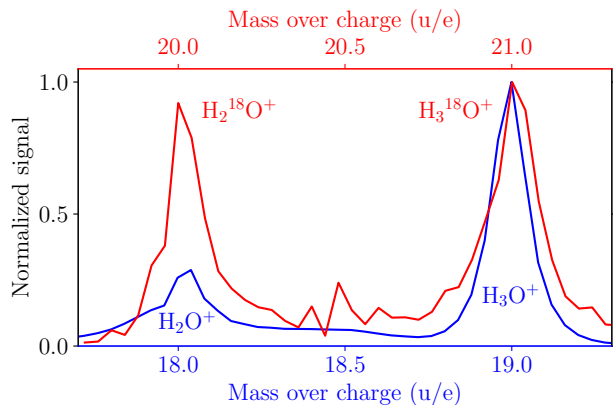


FIG. 4. Comparison of the peak-normalized mass spectra including the signals assigned to (blue)  $H_2O^+$  and  $H_3O^+$ , and (red)  $H_2^{18}O^+$  and  $H_3^{18}O^+$ . The red line is background corrected to exclude the background of the  $H_2^{18}O^+$  peak centered at 20 u/e. This is shown in ?? in SI. See also the text for details on possible small  $^{17}O$  backgrounds.

## CONCLUSIONS

Overall, our study provides unique novel experimental observations of the  $(H_2O)_2^+$  fragmentation pathways, which were previously only, and only partly, predicted by molecular dynamics simulations [15, 16]. These results substantially broaden our perspective on  $(H_2O)_2^+$  fragmentation by showing an additional set of newly observed ion-radical pathways and their relative ion yields. Together with our estimated appearance energies  $E_A$ , these indicate the relative significance among all detected channels.

The observed very strong O-isotope effect indicates non-classical aspects of molecular structure and reactivity in the fragmentation. Together with the experimental information on kinetic energies and angular distributions of all fragments, these data is a very valuable asset for advanced molecular-dynamics simulations unraveling the underlying chemistry. Time-resolved investigations of the ionization and subsequent reaction pathways of water dimer could provide further insight into its electronic and nuclear dynamics, including the timescales of proton and hydrogen transfer, the traversal of electronic states, and electronic relaxation processes.

Our findings are relevant for discussions of the role of water ionization and the produced ionic and radical fragments as triggers of the subsequent ion-radical photochemistry, e. g., on ice mantels of dust particles in interstellar space. They also generally help to disentangle the broad inventory of environmentally important radicals.

## DATA AVAILABILITY

The data that support the findings of this study are available from the corresponding author upon request.

## CODE AVAILABILITY

The scripts used to analyse the recorded data and the specified equations are available from the corresponding author upon request.

## SUPPORTING INFORMATION

Experimental ion-imaging map with the deflector-electrodes grounded; photo-photoion coincidence map; description of a model for calculating the appearance energies; plot of the total-momentum release for specified ions; dependence of the appearance energy on the relative ion yields; details on the correction of the background in the calculations of the  $H_2^{18}O^+/H_3^{18}O^+$  ratio.

## ACKNOWLEDGMENTS

We acknowledge financial support by Deutsches Elektronen-Synchrotron DESY, a member of the Helmholtz Association (HGF), also for the use of the Maxwell computational resources operated at DESY and through the Center for Molecular Water Science (CMWS). This work was further supported by the Matter innovation pool of the Helmholtz Association through the DataX project and through the Helmholtz-Lund International Graduate School (HELIOS, HIRS-0018) and by the federal cluster of excellence “Advanced Imaging of Matter” (AIM, EXC 2056, ID 390715994) of the Deutsche Forschungsgemeinschaft (DFG).

## REFERENCES

- 
- \* jochen.kuepper@cfel.de;  
<https://www.controlled-molecule-imaging.org>  
 † sebastian.trippel@cfel.de
- [1] P. Chýlek and D. Geldart, Water vapor dimers and atmospheric absorption of electromagnetic radiation, *Geophys. Res. Lett.* **24**, 2015 (1997).
  - [2] E. Vogt and H. G. Kjaergaard, Vibrational spectroscopy of the water dimer at jet-cooled and atmospheric temperatures, *Annu. Rev. Phys. Chem.* **73**, 209 (2022).
  - [3] G. K. Schenter, S. M. Kathmann, and B. C. Garrett, Dynamical nucleation theory: A new molecular approach to vapor-liquid nucleation, *Phys. Rev. Lett.* **82**, 3484 (1999).
  - [4] J. M. Anglada and A. Solé, Impact of the water dimer on the atmospheric reactivity of carbonyl oxides, *Phys. Chem. Chem. Phys.* **18**, 17698 (2016).
  - [5] J. Headrick and V. Vaida, Significance of water complexes in the atmosphere, *Phys. Chem. Earth (C)* **26**, 479 (2001).
  - [6] M. Y. Tret'yakov, M. A. Koshelev, E. A. Serov, V. V. Parshin, T. A. Odintsova, and G. M. Bubnov, Water dimer and the atmospheric continuum, *Phys.-Uspekhi* **57**, 1083 (2014).
  - [7] M. Y. Tret'yakov, E. A. Serov, M. A. Koshelev, V. V. Parshin, and A. F. Krupnov, Water dimer rotationally resolved millimeter-wave spectrum observation at room temperature, *Phys. Rev. Lett.* **110**, 093001 (2013).
  - [8] G. C. Molano and I. Kamp, The role of OH in the chemical evolution of protoplanetary disks-I. The comet-forming region, *Astron. Astrophys.* **537**, 138 (2012).
  - [9] D. E. Woon, Quantum Chemical Cluster Studies of Cation-Ice Reactions for Astrochemical Applications: Seeking Experimental Confirmation, *Acc. Chem. Res.* **54**, 490 (2021).
  - [10] F. J. Ciesla, The phases of water ice in the solar nebula, *Astrophys. J. Lett.* **784**, L1 (2014).
  - [11] N. Watanabe and A. Kouchi, Ice surface reactions: A key to chemical evolution in space, *Prog. Surf. Sci.* **83**, 439 (2008).
  - [12] T. Jahnke, H. Sann, T. Havermeier, K. Kreidi, C. Stuck, M. Meckel, M. Schöffler, N. Neumann, R. Wallauer, S. Voss, A. Czasch, O. Jagutzki, A. Malakzadeh, F. Afaneh, T. Weber, H. Schmidt-Böcking, and R. Dörner, Ultrafast energy transfer between water molecules, *Nat. Phys.* **6**, 139 (2010).
  - [13] S. Thürmer, M. Ončák, N. Ottosson, R. Seidel, U. Hergenahhn, S. E. Bradforth, P. Slavíček, and B. Winter, On the nature and origin of dicationic, charge-separated species formed in liquid water on X-ray irradiation, *Nat. Chem.* **5**, 590 (2013).
  - [14] T. Jahnke, Interatomic and intermolecular Coulombic decay: the coming of age story, *J. Phys. B* **48**, 082001 (2015).
  - [15] O. Svoboda, D. Hollas, M. Ončák, and P. Slavíček, Reaction selectivity in an ionized water dimer: Nonadiabatic ab initio dynamics simulations, *Phys. Chem. Chem. Phys.* **15**, 11531 (2013).
  - [16] J. Chalabala, F. Uhlig, and P. Slavíček, Assessment of real-time time-dependent density functional theory (RT-TDDFT) in radiation chemistry: Ionized water dimer, *J. Phys. Chem. A* **122**, 3227 (2018).
  - [17] C. Richter, D. Hollas, C. M. Saak, M. Förstel, T. Miteva, M. Mucke, O. Björneholm, N. Sisourat, P. Slavíček, and U. Hergenahhn, Competition between proton transfer and intermolecular Coulombic decay in water, *Nat. Commun.* **9**, 4988 (2018).
  - [18] T. Takada and H. Tachikawa, Direct ab initio molecular dynamics study on the reactions of multi-valence ionized states of water dimer, *J. Phys. B* **54**, 145103 (2021).
  - [19] C. Zhang, J. Lu, T. Feng, and H. Rottke, Proton transfer dynamics following strong-field ionization of the water dimer, *Phys. Rev. A* **99**, 053408 (2019).
  - [20] D. M. Kramer, T. J. Avenson, and G. E. Edwards, Dynamic flexibility in the light reactions of photosynthesis governed by both electron and proton transfer reactions, *Trends Plant Sci.* **9**, 349 (2004).
  - [21] B. Boudaïffa, P. Cloutier, D. Hunting, M. A. Hues, and L. Sanche, Resonant formation of DNA strand breaks by low-energy (3 to 20 eV) electrons, *Science* **287**, 1658 (2000).
  - [22] G. Hanel, B. Gstir, S. Denifl, P. Scheier, M. Probst, B. Farizon, M. Farizon, E. Illenberger, and T. Märk, Electron attachment to uracil: Effective destruction at subexcitation energies, *Phys. Rev. Lett.* **90**, 188104 (2003).
  - [23] O. Svoboda, M. Ončák, and P. Slavíček, Simulations of light induced processes in water based on ab initio path integrals molecular dynamics. II. Photoionization, *J. Chem. Phys.* **135**, 154302 (2011).
  - [24] U. Buck and M. Winter, Electron bombardment induced fragmentation of size selected neutral  $(D_2O)_n$  clusters, *Z. Phys. D* **31**, 291 (1994).
  - [25] L. C. Ch'ng, A. K. Samanta, G. Czako, J. M. Bowman, and H. Reisler, Experimental and theoretical investigations of energy transfer and hydrogen-bond breaking in the water dimer, *J. Am. Chem. Soc.* **134**, 15430 (2012).
  - [26] K. Schnorr, M. Belina, S. Augustin, H. Lindenblatt, Y. Liu, S. Meister, T. Pfeifer, G. Schmid, R. Treusch, F. Trost, P. Slavíček, and R. Moshhammer, Direct tracking of ultrafast proton transfer in water dimers, *Science Advances* **9**, eadg7864 (2023).
  - [27] H. Bieker, J. Onvlee, M. Johny, L. He, T. Kierspel, S. Trippel, D. A. Horke, and J. Küpper, Pure molecular beam of water dimer, *J. Phys. Chem. A* **123**, 7486 (2019),

- arXiv:1904.08716 [physics].
- [28] H. Bromberger, C. Passow, D. Pennicard, R. Boll, J. Correa, L. He, M. Johny, C. Papadopoulou, A. Tul-Noor, J. Wiese, S. Trippel, B. Erk, and J. Küpper, Shot-by-shot 250 kHz 3D ion and MHz photoelectron imaging using Timepix3, *J. Phys. B* **55**, 144001 (2022), arXiv:2111.14407 [physics].
- [29] C. Cheng, G. Moğol, T. Weinacht, A. Nomerotski, and C. Trallero-Herrero, 3D velocity map imaging of electrons with TPX3CAM, *Rev. Sci. Instrum.* **93**, 013003 (2022).
- [30] M. Brouard, E. Halford, A. Lauer, C. Slater, B. Winter, W. Yuen, J. John, L. Hill, A. Nomerotski, A. Clark, *et al.*, The application of the fast, multi-hit, pixel imaging mass spectrometry sensor to spatial imaging mass spectrometry, *Rev. Sci. Instrum.* **83**, 114101 (2012).
- [31] Y.-P. Chang, D. A. Horke, S. Trippel, and J. Küpper, Spatially-controlled complex molecules and their applications, *Int. Rev. Phys. Chem.* **34**, 557 (2015), arXiv:1505.05632 [physics].
- [32] W. Jin, S. Trippel, J. Küpper, *et al.*, eCOMO, a new endstation for controlled molecule experiments (2023), in preparation.
- [33] S. Trippel, M. Johny, T. Kierspel, J. Onvlee, H. Bieker, H. Ye, T. Mullins, L. Gumprecht, K. Długołęcki, and J. Küpper, Knife edge skimming for improved separation of molecular species by the deflector, *Rev. Sci. Instrum.* **89**, 096110 (2018), arXiv:1802.04053 [physics].
- [34] D. Irimia, D. Dobrikov, R. Kortekaas, H. Voet, D. A. van den Ende, W. A. Groen, and M. H. M. Janssen, A short pulse (7  $\mu$ s FWHM) and high repetition rate (dc–5kHz) cantilever piezovalve for pulsed atomic and molecular beams, *Rev. Sci. Instrum.* **80**, 113303 (2009).
- [35] J. S. Kienitz, K. Długołęcki, S. Trippel, and J. Küpper, Improved spatial separation of neutral molecules, *J. Chem. Phys.* **147**, 024304 (2017), arXiv:1704.08912 [physics].
- [36] J. K. Gregory, The dipole moment of the water dimer, *Chem. Phys. Lett.* **282**, 147 (1998).
- [37] J. K. Gregory, D. C. Clary, K. Liu, M. G. Brown, and R. J. Saykally, The water dipole moment in water clusters, *Science* **275**, 814 (1997).
- [38] K. B. Snow and T. F. Thomas, Mass spectrum, ionization potential, and appearance potentials for fragment ions of sulfuric acid vapor, *Int. J. Mass Spectrom.* **96**, 49 (1990).
- [39] A. T. J. B. Eppink and D. H. Parker, Velocity map imaging of ions and electrons using electrostatic lenses: Application in photoelectron and photofragment ion imaging of molecular oxygen, *Rev. Sci. Instrum.* **68**, 3477 (1997).
- [40] A. Zhao, M. van Beuzekom, B. Bouwens, D. Byelov, I. Chakaberia, C. Cheng, E. Maddox, A. Nomerotski, P. Svihra, J. Visser, V. Vrba, and T. Weinacht, Coincidence velocity map imaging using Tpx3Cam, a time stamping optical camera with 1.5 ns timing resolution, *Rev. Sci. Instrum.* **88**, 113104 (2017), arXiv:1707.06253 [physics].
- [41] A. Al-Refaie, M. Johny, J. Correa, D. Pennicard, P. Svihra, A. Nomerotski, S. Trippel, and J. Küpper, PymePix: A python library for SPIDR readout of Timepix3, *J. Instrum.* **14** (10), P10003, arXiv:1905.07999 [physics].
- [42] CFEL Controlled Molecule Imaging, PymePix, Code repository, URL: <https://github.com/CFEL-CMI/pymepix> (2020).
- [43] B. Whitaker, *Imaging in Molecular Dynamics: Technology and Applications* (Cambridge University Press, Cambridge, UK, 2003).
- [44] Scientific Instrument Services Inc., USA, Simion 8.1 (2011), URL: <http://simion.com>.
- [45] M. V. Ammosov, N. B. Delone, and V. P. Krainov, Tunnel ionization of complex atoms and of atomic ions in an alternating electromagnetic field, *Sov. Phys. JETP* **64**, 1191 (1986).



***Supporting Information for Publication:***  
**Reaction Pathways of Water Dimer Following Single Ionization**

Ivo S. Vinklársek,<sup>1</sup> Hubertus Bromberger,<sup>1</sup> Nidin Vadassery,<sup>1</sup>  
 Wuwei Jin,<sup>1</sup> Jochen Küpper,<sup>1,2,3,\*</sup> and Sebastian Trippel<sup>1,2,†</sup>

<sup>1</sup>*Center for Free-Electron Laser Science CFEL, Deutsches  
 Elektronen-Synchrotron DESY, Notkestr. 85, 22607 Hamburg, Germany*

<sup>2</sup>*Center for Ultrafast Imaging, Universität Hamburg, Luruper Chaussee 149, 22761 Hamburg, Germany*

<sup>3</sup>*Department of Physics, Universität Hamburg, Luruper Chaussee 149, 22761 Hamburg, Germany*

(Dated: 2024-03-18)

<b>CONTENTS</b>			
List of Figures	S1	S2	Photoion-photoion correlation . . . . . S2
List of Tables	S1	S3	Total-momentum releases . . . . . S3
Model	S2	S4	Appearance energies . . . . . S3
Experimental results	S3	S5	Isotopologue intensities . . . . . S4
Ratio of H <sub>2</sub> <sup>18</sup> O <sup>+</sup> /H <sub>3</sub> <sup>18</sup> O <sup>+</sup>	S3	S6	Background correction . . . . . S4
References	S4		

<b>LIST OF FIGURES</b>			<b>LIST OF TABLES</b>	
S1	Map of the ion signal without deflection	S2	S1	Branching ratios . . . . . S2

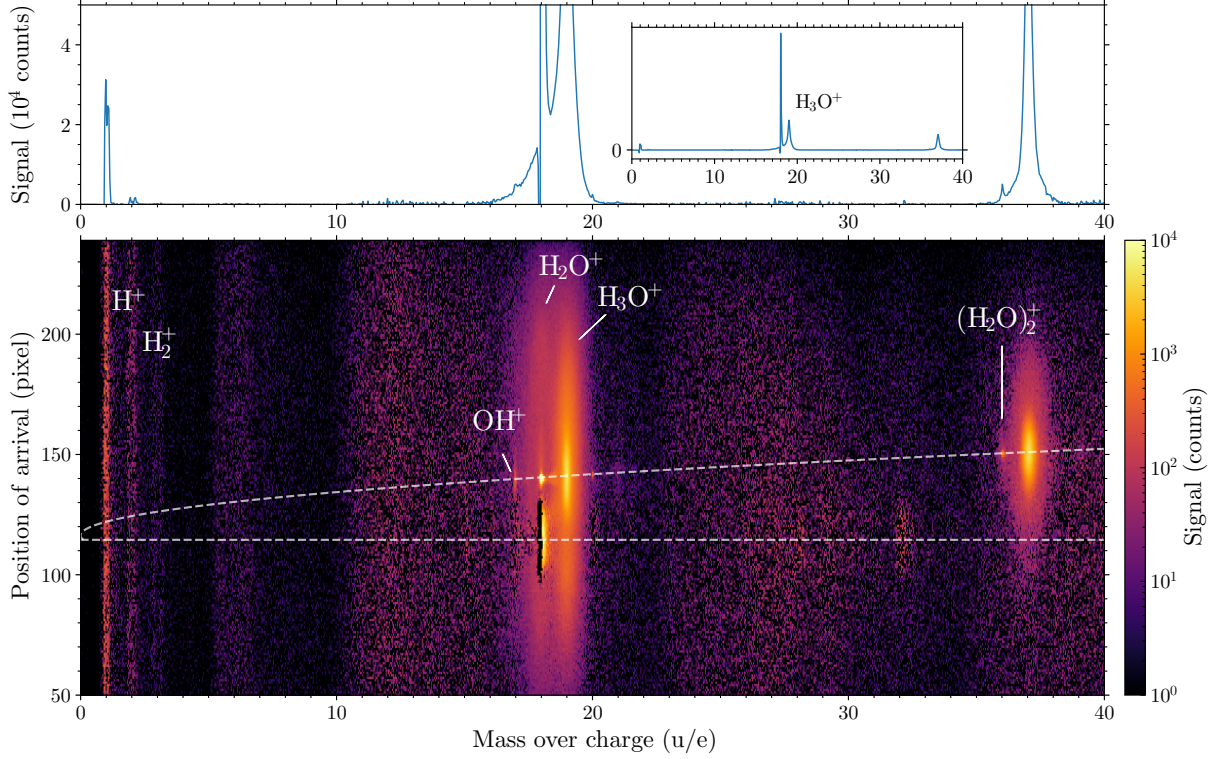


Figure S1. Image mapping the ion signal according to the mass-over-charge ratio and the position of arrival at the detector. This two-dimensional spectrum was obtained with deflector off.

### MODEL

To estimate the appearance energies for ions with low abundances, i. e.,  $O_2^+$ ,  $HO_2^+$ ,  $(H_2O-O)^+$ ,  $H_2^+$ , and  $H_3^+$ , we designed a semi-empirical model combining the measured relative ion yields with reported ionization energies  $E_i$  and branching ratios [1]. For the calculation of the ion yield of  $I^+$  we applied the equation

$$P(I^+) = N \cdot \sum_k y_k^S(I^+) \cdot D(F, E_i(S)), \quad (1)$$

where  $N$  is a normalization factor,  $y_k^S$  is the branching ratio of the channel  $k$  after ionization into state  $S$  and  $D$  is a distribution describing the ionization probability.  $D$  depends on the parameter  $F$  corresponding to the strength of the applied external field [2] and the ionization energy  $E_i(S)$  of state  $S$ . (1) was rewritten into the following equations using the reported

TABLE S1. Comparison of the measured and calculated branching ratios for the selected ions.

Ion	$H_3O^+$	$H_2O^+$	$(H_2O)_2^+$	$H^+$	$OH^+$
Measured	0.541	0.176	0.172	0.060	0.032
Calculated	0.494	0.180	0.233	0.061	0.033

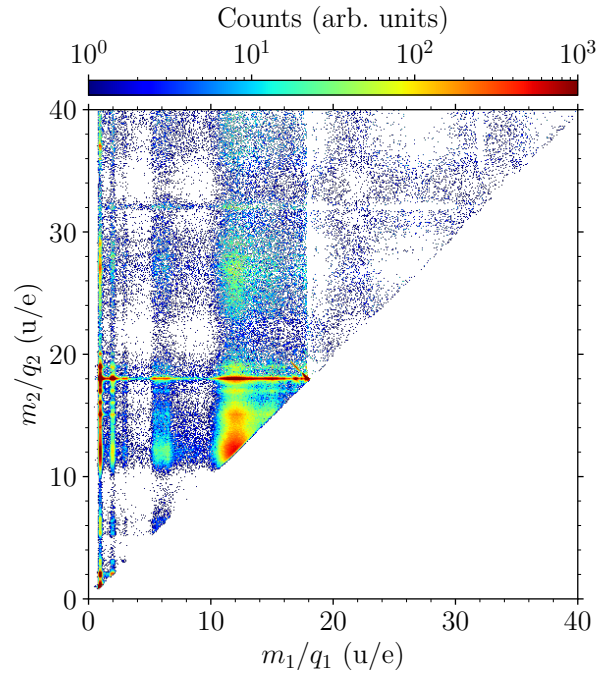


Figure S2. Photoion-photoion correlation for the mass-over-charge range between 0 and 40.

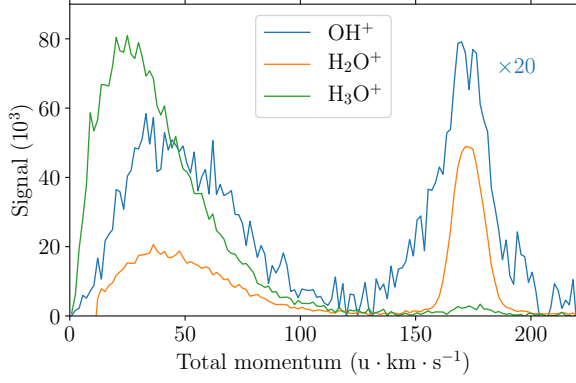


Figure S3. Total-momentum release of the reaction channels yielding the specified ions with the assumption of two-body fragmentation.

parameters [1]

$$P(\text{H}_3\text{O}^+) = N \cdot (D(F, 11.7) \cdot 0.635 + D(F, 12.8) \cdot 0.66 + D(F, 18.2) \cdot 0.14), \quad (2)$$

$$P((\text{H}_2\text{O})_2^+) = N \cdot (D(F, 11.7) \cdot 0.365 + D(F, 12.8) \cdot 0.245), \quad (3)$$

$$P(\text{H}_2\text{O}^+) = N \cdot (D(F, 12.8) \cdot 0.095 + D(F, 18.2) \cdot 0.86 + D(F, 18.5) \cdot (1 - p_{\text{OH}^+}) + D(F, 19.2) \cdot (1 - p_{\text{H}^+})), \quad (4)$$

$$P(\text{OH}^+) = N \cdot (D(F, 18.5) \cdot p_{\text{OH}^+}), \quad (5)$$

$$P(\text{H}^+) = N \cdot (D(F, 19.2) \cdot p_{\text{H}^+}). \quad (6)$$

The parameters  $F$ ,  $p_{\text{OH}^+}$ , and  $p_{\text{H}^+}$  were optimized to fit the measured and calculated relative ion yields. Assuming  $D(F, E_i) = \exp(-E_i/F)$ , this yielded  $F = 4.34$  eV,  $p_{\text{OH}^+} = 0.37$  and  $p_{\text{H}^+} = 0.82$ . The calculated and measured relative ion yields are shown in the Table S1. The fitted field-strength parameter  $F$  was then applied to estimate appearance energies  $E_A$  of other ions  $\text{I}^+$  with low abundance according to

$$E_A^{\text{I}^+} = -F \cdot \log(P(\text{I}^+)) \quad (7)$$

where we set branching ratio equal to 1. The evaluated appearance energies are shown in the fourth column of Table 1 in the main text.

Finally, we would like to point out that the fitted value of  $F = 4.34$  eV corresponding to the strength of the applied external field agrees well with the ponderomotive energy  $U_p$  multiplied by  $1/e$ , i. e.,

$$U_p = \frac{E_i}{2\gamma^2} \cdot \frac{1}{e} = 4.39 \text{ eV}, \quad (8)$$

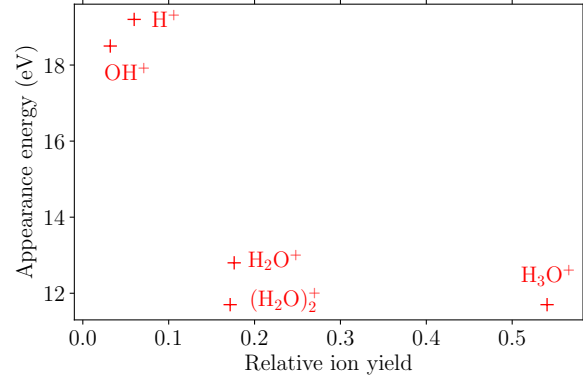


Figure S4. Dependence of the appearance energy  $E_A$  on the relative ion yields for  $\text{H}_3\text{O}^+$ ,  $\text{H}_2\text{O}^+$ ,  $(\text{H}_2\text{O})_2^+$ ,  $\text{OH}^+$ , and  $\text{H}^+$  ions.

$E_i$  is the ionization energy of water dimer (11.7 eV) and  $\gamma = 0.7$  the corresponding Keldysh parameter. Thus, it is tempting to assign a real physical meaning to the parameter  $F$  as the ‘‘averaged’’ ponderomotive energy. Nevertheless, further modelling of our experiment is necessary to confirm this hypothesis.

## EXPERIMENTAL RESULTS

Here, we provide additional information on the experimental results discussed in the main text. Figure S1 displays the acquired background-subtracted ion signal with the deflector off ( $U_d = 0$  kV). The acquired signal illustrates the direct-molecular-beam background of our measurement. Figure S2 shows results of our photoion-photoion covariance analysis for the mass-over-charge range between 0 and 40. The fact that there are no cross-correlation peaks for the range 32–34 u/e support the origin of the  $\text{O}_2^+$ ,  $\text{HO}_2^+$  and  $(\text{H}_2\text{O}-\text{O})^+$  ions in the  $(\text{H}_2\text{O})_2^+$  fragmentation.

Figure S3 shows the total-momentum release for the specified ions following strong-field ionization of  $(\text{H}_2\text{O})_2$ . Figure S4 shows the correlation between the reported appearance energies  $E_A$  and the measured relative ion yields.

## RATIO OF $\text{H}_2^{18}\text{O}^+/\text{H}_3^{18}\text{O}^+$

The ion count ratios of  $\text{H}_2\text{O}^+/\text{H}_3\text{O}^+ \approx 3$  and  $\text{H}_2^{18}\text{O}^+/\text{H}_3^{18}\text{O}^+ \approx 1$ , discussed in the main text, are determined from the signals plotted in Figure 1 in the main text. The ratios indicate different dynamics for the respective  $^{18}\text{O}$  and  $^{16}\text{O}$  isotopologues. Figure S5 shows the ion-imaging maps in the areas of the  $\text{H}_2^{18}\text{O}^+$  and  $\text{H}_3^{18}\text{O}^+$  signals together with the region of interests used to obtain the ion counts, i. e., 10225 and 9225, respectively. This was further supported by the areas in the mass spectrum corrected for the signal

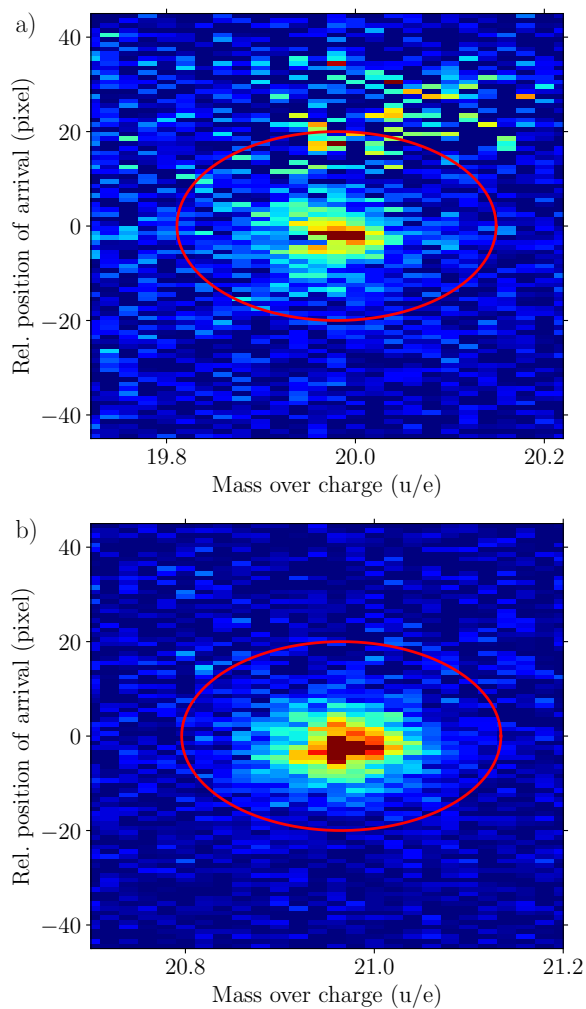


Figure S5. Ion-imaging maps for (a)  $\text{H}_2^{18}\text{O}^+$  and (b)  $\text{H}_3^{18}\text{O}^+$  signals with the regions of interest used for the ion counting marked by red ellipses.

due to the broad distribution of the  $\text{H}_3\text{O}^+$  peak, see Figure S6.

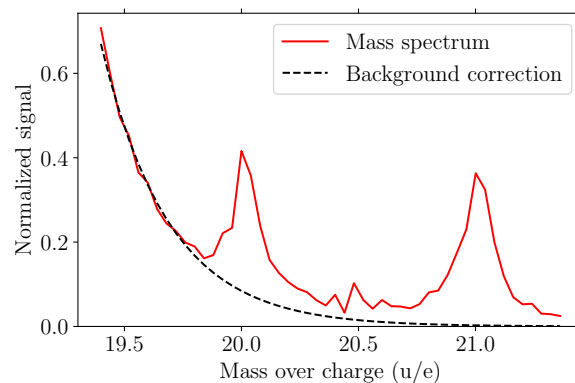


Figure S6. Mass spectrum in the  $^{18}\text{O}$ -isotopologue range with the fitted background from  $^{16}\text{O}$  isotopologues.

\* Email: jochen.kuepper@cfel.de

† Email: sebastian.trippel@cfel.de;

Website: <https://www.controlled-molecule-imaging.org>

- [1] O. Svoboda, D. Hollas, M. Ončák, and P. Slavíček, Reaction selectivity in an ionized water dimer: Nonadiabatic ab initio dynamics simulations, *Phys. Chem. Chem. Phys.* **15**, 11531 (2013).
- [2] M. V. Ammosov, N. B. Delone, and V. P. Krainov, Tunnel ionization of complex atoms and of atomic ions in an alternating electromagnetic field, *Sov. Phys. JETP* **64**, 1191 (1986).